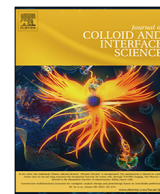




Contents lists available at ScienceDirect

Journal of Colloid and Interface Science

journal homepage: www.elsevier.com/locate/jcis

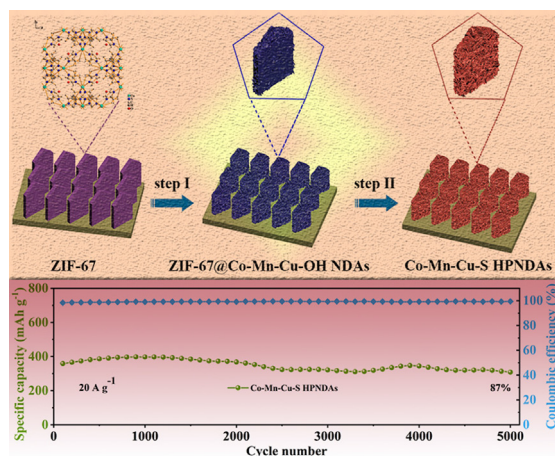
Engineering hierarchical porous ternary Co-Mn-Cu-S nanodisk arrays for ultra-high-capacity hybrid supercapacitors

Wuquan Ye^a, Pengcheng Ye^a, Haiyan Wang^{a,*}, Fang Chen^b, Yijun Zhong^a, Yong Hu^{a,b,*}

^a Key Laboratory of the Ministry of Education for Advanced Catalysis Materials, Department of Chemistry, Zhejiang Normal University, Jinhua 321004, China

^b Hangzhou Institute of Advanced Studies, Zhejiang Normal University, Hangzhou 311231, China

GRAPHICAL ABSTRACT



ARTICLE INFO

Article history:

Received 5 November 2021

Revised 21 December 2021

Accepted 23 December 2021

Available online 28 December 2021

Keywords:

Co-Mn-Cu-S

Nanodisk arrays

Hierarchical porous structure

Ultra-high capacity

Hybrid supercapacitors

ABSTRACT

Transition-metal sulfides have been recognized as one of the promising electrodes for high-performance hybrid supercapacitors (HSCs). However, the poor rate performance and short cycle life heavily impede their practical applications. Herein, an advanced electrode based on hierarchical porous cobalt-manganese-copper sulfide nanodisk arrays (Co-Mn-Cu-S HPNDAs) on Ni foam is fabricated for high-capacity HSCs, using metal-organic frameworks as the self-sacrificial template. The synergistic effects of ternary Co-Mn-Cu sulfides and the hierarchical porous structure endow the as-obtained electrode with fast redox reaction kinetics. As expected, the resultant Co-Mn-Cu-S HPNDAs electrode delivers an ultra-high specific capacity of 536.8 mAh g⁻¹ (3865 F g⁻¹) at 2 A g⁻¹ with a superb rate performance of 63% capacity retention at 30 A g⁻¹. Remarkably, an energy density of 63.8 W h kg⁻¹ at a power density of 743 W kg⁻¹ with a long cycle life is also achieved with the quasi-solid-state Co-Mn-Cu-S HPNDAs//ZIF-8-derived carbon HSC. This work offers a new pathway to fabricate high-performance multiple transition-metal-sulfide-based electrode materials for energy storage devices.

© 2021 Elsevier Inc. All rights reserved.

* Corresponding authors at: Key Laboratory of the Ministry of Education for Advanced Catalysis Materials, Department of Chemistry, Zhejiang Normal University, Jinhua 321004, China (Y. Hu).

E-mail addresses: chemwhy@zjnu.edu.cn (H. Wang), yonghu@zjnu.edu.cn (Y. Hu).

<https://doi.org/10.1016/j.jcis.2021.12.159>

0021-9797/© 2021 Elsevier Inc. All rights reserved.

1. Introduction

Supercapacitors have received intense interests as energy storage technologies due to high power density that is about 100 times higher than Li-ion batteries, fast charge and discharge rate, long cycle life, and high safety [1,2]. Hence, they have been served as

back-up power systems to complement batteries in hybrid vehicles [3]. The bottleneck still is the low energy density, which seriously impedes their development. In this regard, hybrid supercapacitors (HSCs) that couple electrical double-layer capacitive materials with pseudocapacitive or battery-type materials offer a favorable choice by providing a larger capacitance and extending the output voltage window meanwhile [4–6].

To this end, various kinds of pseudocapacitive and battery-type materials have been diffusely studied in the past decades. Transition metal sulfides, especially cobalt sulfides have been demonstrated promising candidates for HSCs as they possess the merits of high theoretical specific capacitance, excellent electrical conductivity, thermal stability, and complex redox reactions [7,8]. The low electronegativity of sulfur can help maintain the structural integrity through reducing structure expansions, and therefore boosts the mechanical flexibility [9]. However, they usually suffer from poor rate capability and limited cyclic life [10]. The key to solving the problems is to accelerate electron/electrolyte transport in the electrode materials. Among these strategies, introduction of hetero-metal to adjust the surface reactivity is an effective method to enhance the electrochemical properties [11]. In particular, cobalt-manganese or cobalt-copper sulfides have been received considerable research attention due to their multiple valence states, but the results were not so satisfied. According to the previous studies, the introduction of manganese could improve the rate capability of redox electrode materials [12,13], while the copper ions might improve the conductivity [14,15]. Therefore, it is essential to fabricate a ternary cobalt-manganese-copper sulfide system to synergistically enhance the electrochemical performance.

Metal-organic frameworks (MOFs) provide ideal precursors for constructing multi-elemental materials with hierarchical porous nanostructures, which contributes to mass transport [16–18]. By tuning the metal clusters and organic ligands, a variety of MOF-derived transition metal sulfides with different nanostructures have been used as high-performance electrode materials for SCs, such as Ni-Co sulfide nanocages [19], Ni sulfide nanorods [20], Co sulfide nanoarrays [21], and Zn-Co sulfide nanosheet arrays [22]. The direct growth of MOFs arrays on conductive substrates is critical to avoid the agglomeration, which can effectively increase the utilization of the electroactive materials [23]. Nevertheless, there are relatively few reports on MOF-derived ternary transition metal sulfides with a unique 3D hierarchical porous structure. The challenge is the precise and controllable conversion of the MOF templates to guarantee good compatibility of the electrode materials.

In this study, we for the first time demonstrate that the introduction of manganese and copper can significantly improve the charge storage performance of cobalt sulfides. A facile self-templated strategy is developed for the in-situ synthesis of hierarchical porous cobalt-manganese-copper sulfide nanodisk arrays (denoted as Co-Mn-Cu-S HPNDAs) on nickel foam (NF). The Co-Mn-Cu-S HPNDAs electrode delivers an ultrahigh specific capacity of 536.8 mAh g⁻¹ (3865 F g⁻¹) at 2 A g⁻¹, and excellent rate performance with 63% capacity retention at 30 A g⁻¹, which surpasses cobalt sulfide nanodisk arrays (Co-S NDAs), hierarchical porous cobalt-copper sulfide nanodisk arrays (Co-Cu-S HPNDAs) and hierarchical porous cobalt-manganese sulfide nanodisk arrays (Co-Mn-S HPNDAs). The superior performance of the Co-Mn-Cu-S HPNDAs can be ascribed to the structural merits and synergistic effect of ternary Co-Mn-Cu-S components. Furthermore, the quasi-solid-state HSC assembled with Co-Mn-Cu-S HPNDAs and MOF-derived nanoporous carbon (NPC) presents a maximum energy density of 63.8 W h kg⁻¹ at a power density of 743 W kg⁻¹, and prominent cycling stability without degradation after 5000 cycles. This work can provide a direction for constructing MOF-based hierarchical porous nanoarrays of ternary chalcogenides in other related energy storage fields.

2. Experiments

2.1. In-situ growth of ZIF-67 on NF

40 mL of aqueous Co(NO₃)₂·6H₂O solution (50 mM) was poured into an aqueous solution (40 mL) containing 2-methylimidazole (MIM, 0.4 M) in a 100 mL of beaker. After sonication for 10 min, a piece of NF (3 × 4 cm²) was put into the above solution for 1.5 h at room temperature. Then the NF coated with ZIF-67 was washed with deionized water and ethanol, and dried at 60 °C overnight.

2.2. Preparation of ZIF-67@Co-Mn-Cu-OH NDAs

A piece of NF coated with ZIF-67 was immersed into a mixed solution containing 50 mL of aqueous Mn(CH₃COO)₂·4H₂O solution (30 mM) and 50 mL of aqueous CuSO₄·5H₂O solution (10 mM). After 5 min later, the NF was washed with deionized water and ethanol, and then dried at 60 °C overnight. The obtained product is denoted as ZIF-67@cobalt-manganese-copper hydroxide nanodisk arrays (ZIF-67@Co-Mn-Cu-OH NDAs).

For comparison, ZIF-67@cobalt-copper hydroxide nanodisk arrays (ZIF-67@Co-Cu-OH NDAs) and ZIF-67@cobalt-manganese hydroxide nanodisk arrays (ZIF-67@Co-Mn-OH NDAs) were synthesized with the same procedure of ZIF-67@Co-Mn-Cu-OH NDAs, but without the addition of Mn(CH₃COO)₂·4H₂O and CuSO₄·5H₂O, respectively.

2.3. Preparation of Co-Mn-Cu-S HPNDAs

A NF coated with ZIF-67@Co-Mn-Cu-OH NDAs was put into an ethanol solution (40 mL) that contains 1.6 mmol of thioacetamide (TAA), and was then transferred into a Teflon-lined autoclave at 120 °C for 4 h. The NF coated with Co-Mn-Cu-S HPNDAs was washed with deionized water and ethanol, and dried at 60 °C overnight.

For comparison, Co-S NDAs was synthesized through sulfidation of ZIF-67 at 120 °C for 4 h with TAA as the sulfur source. Co-Cu-S HPNDAs and Co-Mn-S HPNDAs were also prepared with the same procedure above by using ZIF-67@Co-Cu-OH NDAs and ZIF-67@Co-Mn-OH NDAs as the precursor, respectively. The mass loading of samples was 1.5 mg cm⁻² ~ 2.0 mg cm⁻².

2.4. Preparation of MOF-derived NPC

The MOF-derived NPC was prepared according to the previous report [24,25]. Typically, 48 mM Zn(CH₃COO)₂·2H₂O was added into a 200 mL of methanol solution containing 0.4 mM polyvinyl pyrrolidone (PVP, K30) to prepare the solution A. Next, the solution A was mixed with another methanol solution (200 mL) containing 160 mM MIM, and stirred for 1 h. After 24 h, the ZIF-8 was obtained with centrifugation and washed. MOF-derived NPC was prepared by calcination of ZIF-8 at 900 °C for 5 h under N₂ atmosphere.

The details for materials characterizations, electrochemical measurements, and fabrication of the quasi-solid-state HSC can be seen in the [supporting information](#).

3. Results and discussion

The synthesis process of Co-Mn-Cu-S HPNDAs is presented in Fig. 1. Uniform ZIF-67 nanoarrays are first grown on the NF through the coordination between cobalt ions and MIM ligand. Subsequently, the ZIF-67 nanoarrays are etched by the Mn²⁺ and Cu²⁺ ions and meanwhile, the Co-Mn-Cu-OH nanosheets are

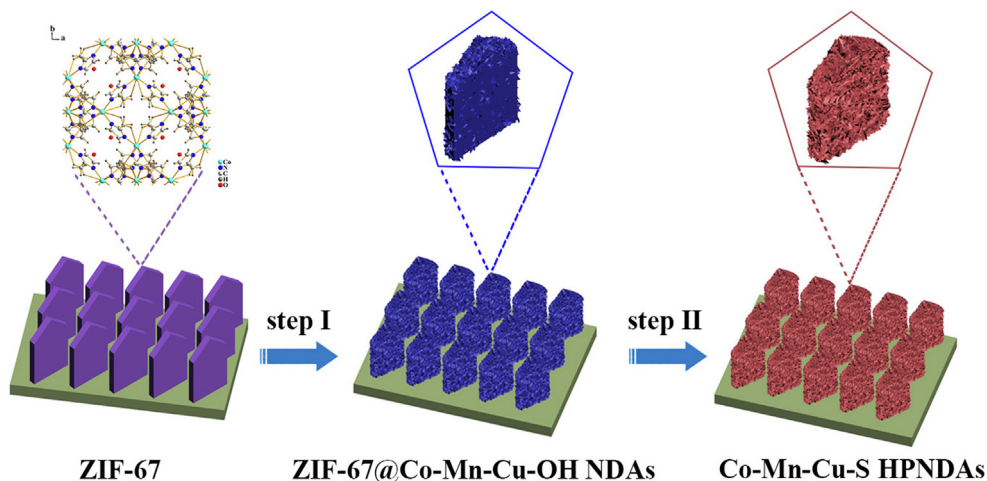


Fig. 1. Synthetic procedure of the Co-Mn-Cu-S HPNDAs.

deposited on the surface of ZIF-67 arrays. As a result, the ZIF-67@Co-Mn-Cu-OH NDAs with a core-shell structure are obtained.

As shown in Fig. S1, the bright purple NF turns dull purple, demonstrating the successful conversion of ZIF-67@Co-Mn-Cu-OH NDAs.

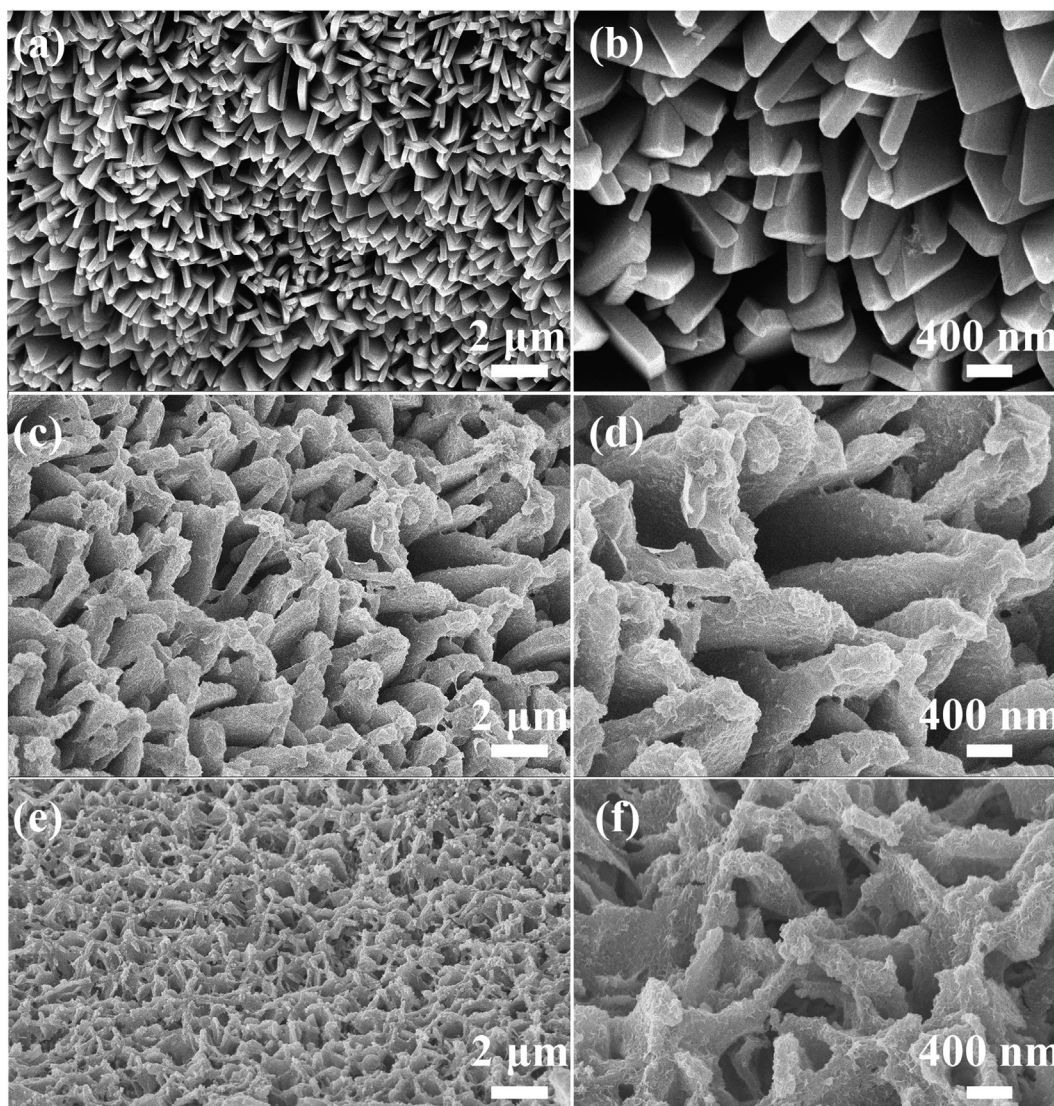


Fig. 2. FESEM images of the as-prepared (a, b) ZIF-67, (c, d) ZIF-67@Co-Mn-Cu-OH NDAs, and (e, f) Co-Mn-Cu-S HPNDAs.

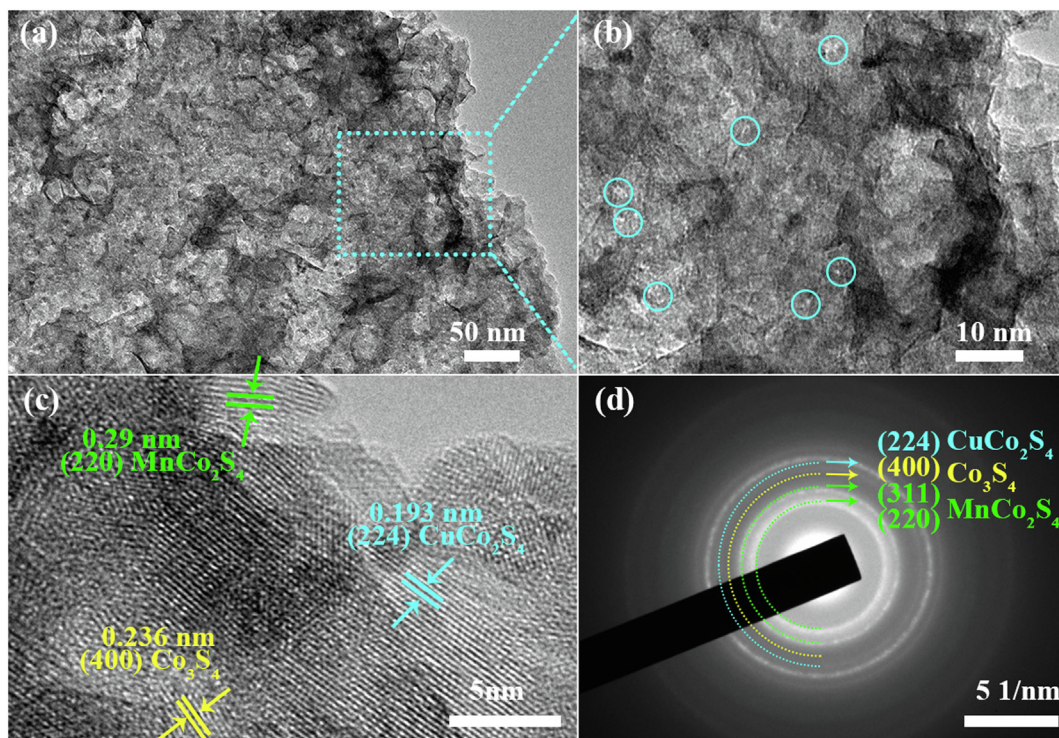


Fig. 3. (a, b) TEM images, (c) HRTEM image, and (d) SAED pattern of the Co-Mn-Cu-S HPNDAs.

Finally, after a sulfidation process with TAA, black Co-Mn-Cu-S with hierarchical porous nanodisk array architecture is achieved.

The morphological evolution from ZIF-67 to Co-Mn-Cu-S HPNDAs was then monitored by field emission scanning electron microscopy (FESEM) and X-ray powder diffraction (XRD). As presented in Fig. 2a and 2b, uniform pentagonal nanodisk arrays of ZIF-67 with an average thickness of about 200 nm on NF substrate is observed. The corresponding XRD pattern is displayed in Fig. S2, which consists well with the ZIF-67 reported previously, verifying the formation of pure ZIF-67 [26,27]. After the process of ion exchange/etching, the pentagonal nanodisk structure of ZIF-67 is maintained, yet the thickness of ZIF-67 nanodisk becomes thinner, and the edge and corner become fuzzier (Fig. 2c and 2d). Clearly observation shows that numerous Co-Mn-Cu-OH nanosheets are arranged on the surface of ZIF-67 nanodisks, resulting in a rough surface. The XRD pattern of the ZIF-67@Co-Mn-Cu-OH NDAs shows the characteristic diffraction peaks of ZIF-67. In addition to these peaks, the small peaks at 34.9°, 39.4°, 60.9° and 62.4° are assigned to the (012), (015), (110) and (113) planes of CoMn LDH (JCPDS NO.40-0216), respectively [28,29], while peaks at 38.5°, 52.5° and 64.9° correspond well to the (150), (−431) and (280) planes of CoCu LDH (JCPDS NO.29-1416), respectively [30]. The formation of the Co-Mn-Cu-OH nanosheets is due to the co-precipitation of Co^{2+} , Mn^{2+} and Cu^{2+} ions. Furthermore, after a sulfidation procedure with TAA, the ZIF-67@Co-Mn-Cu-OH NDAs were converted into Co-Mn-Cu-S and their nanodisk structure was maintained (Fig. 2e and 2f). Elemental mapping indicates that Mn, Cu, Co and S elements are homogeneously distributed in whole nanodisk (Fig. S3). As shown in the XRD pattern (Fig. S4), the main diffraction peaks at 31.36°, 38.05°, 50.25° and 55.00° are assigned to the (311), (400), (511) and (440) planes of Co_3S_4 (JCPDS NO.42-1448). In addition to peaks of Co_3S_4 , characteristic peaks of MnCo_2S_4 (JCPDS NO.23-1237) [31] and CuCo_2S_4 (JCPDS NO.42-1450) can be found, which demonstrate that the sample is composed of Co_3S_4 , MnCo_2S_4 and CuCo_2S_4 composites. The diffraction peaks at

19.62° and 21.98° are ascribed to sulfur (JCPDS NO.24-1251) from TAA decomposition [32,33].

To highlight the advantages of Co-Mn-Cu-S HPNDAs, some contrast samples were prepared. Co-S NDAs was synthesized through sulfidation of ZIF-67 at 120 °C for 4 h with TAA as the sulfur source. Co-Cu-S HPNDAs and Co-Mn-S HPNDAs were also prepared with the same procedure to Co-Mn-Cu-S HPNDAs, but without the addition of manganese salt and copper salt, respectively. The XRD patterns all demonstrate the successful synthesis of Co-S, Co-Cu-S, and Co-Mn-S samples (Fig. S4). The morphologies of the control samples of Co-Mn-S HPNDAs, Co-Cu-S HPNDAs and Co-S NDAs are presented in Fig. S5-S7. It can be seen that Co-S NDAs and Co-Cu-S HPNDAs preserve the nanodisk structure intactly, whereas the nanodisks of the Co-Mn-S are etched seriously. To exclude the effects of the type of anions and the concentration of the additional metal salts, 30 mM $\text{Mn}(\text{CH}_3\text{COO})_2$ is replaced by 10 mM MnSO_4 in the synthesis of the Co-Mn-S HPNDAs. As shown in Fig. S8, the product shows the similar morphology with the Co-Mn-S HPNDAs, indicating that the anions and the concentrations of manganese salts have no influence on the morphology of the as-obtained sample. Hence, the highly etched morphology of Co-Mn-S HPNDAs is due to the stronger etching degree of Mn^{2+} ions compared to Cu^{2+} ions.

The hierarchical porous architecture of Co-Mn-Cu-S HPNDAs was further verified by transmission electron microscopy (TEM) and high-resolution TEM (HRTEM). The TEM image clearly demonstrates that the nanodisk is composed of ultrathin mesoporous nanosheets (Fig. 3a). Furthermore, the magnified image also manifests the existence of micropores in the nanosheet (Fig. 3b). This combined with the above demonstrates that the hierarchical pore structure of Co-Mn-Cu-S HPNDAs contains mesopores and micropores. HRTEM image exhibits the distinct lattice fringes of 0.236 nm, 0.193 nm and 0.29 nm, which corresponds to (400) plane of Co_3S_4 , (224) plane of CuCo_2S_4 and (220) plane of MnCo_2S_4 , respectively (Fig. 3c) [13,31]. The selected area electron diffraction (SAED) pattern shows several concentric rings, verifying the polycrystalline

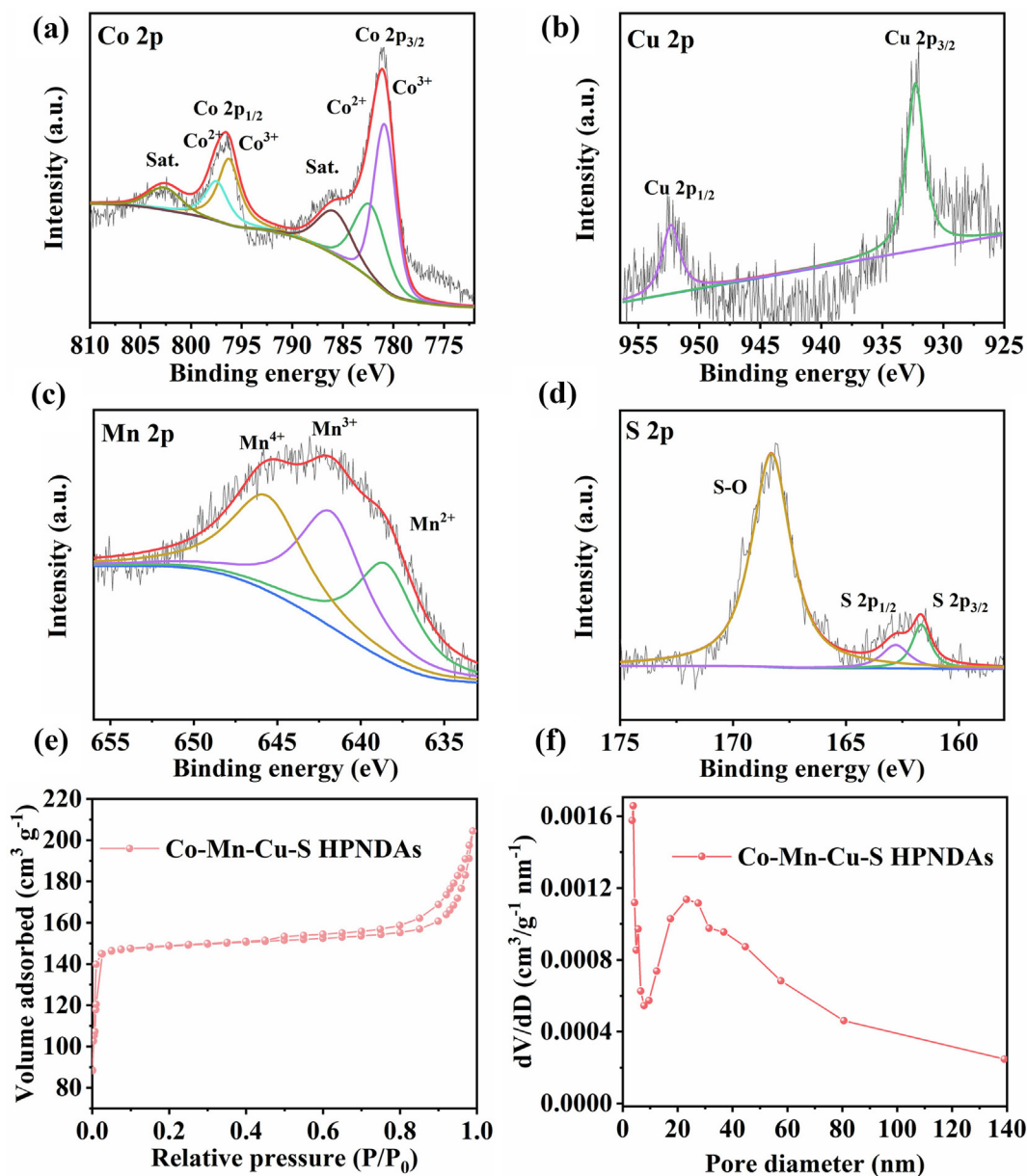


Fig. 4. XPS spectra of (a) Co 2p, (b) Cu 2p, (c) Mn 2p and (d) S 2p for the Co-Mn-Cu-S HPNDAs. (e) N_2 adsorption-desorption isotherms and (f) pore-size distribution curve of the Co-Mn-Cu-S HPNDAs.

nature of Co_3S_4 , $CuCo_2S_4$ and $MnCo_2S_4$ in the Co-Mn-Cu-S HPNDAs sample (Fig. 3d). The metal-ion contents of all samples are determined by inductively coupled plasma atomic emission spectroscopy (ICP). As shown in Table S1, the atomic content of Co in the Co-S NDAs is about 39.86%, which consists well with the Co_3S_4 . In addition, Co-Mn-Cu-S HPNDAs contain 31.71% of Co, 2.15% of Mn and 9.71% of Cu. The atomic ratio of Mn and Cu in Co-Mn-Cu-S HPNDAs is about 1:5. Besides, the contents of Mn and Cu in Co-Mn-Cu-S HPNDAs are similar to those of Co-Mn-S HPNDAs and Co-Cu-S HPNDAs, respectively.

X-ray photoelectron spectroscopy (XPS) measurements were carried out to explore the chemical compositions and elemental states of Co-Mn-Cu-S HPNDAs. The survey spectrum only shows the characteristic peaks of Co 2p, Cu 2p, Mn 2p, O 1s and S 2p, indicating the synthesis of pure Co-Mn-Cu-S (Fig. S9). The high-resolution XPS spectrum of Co 2p can be fitted into two spin-orbit doublets and two shake-up satellites (Fig. 4a). The peaks

located at 796.2 eV and 780.8 eV are assigned to Co $2p_{1/2}$ and Co $2p_{3/2}$ orbitals of Co^{3+} , while the peaks at 797.5 eV and 782.3 eV are associated with Co^{2+} , further indicating the coexistence of Co^{3+} and Co^{2+} in the sample [7]. The Cu 2p XPS spectrum is fitted to two peaks at 952.3 eV and 932.2 eV, which are attributed to Cu^+ (Fig. 4b) [34–36]. In terms of Mn 2p spectrum, the major three peaks at 645.6 eV, 641.8 eV and 638.5 eV originate from Mn^{4+} , Mn^{3+} and Mn^{2+} , respectively (Fig. 4c) [37–40]. Meanwhile, the high-resolution S 2p spectrum reveals the characteristic peaks at 162.8 eV and 161.7 eV that can be ascribed to the S $2p_{1/2}$ and S $2p_{3/2}$ of S^{2-} , respectively (Fig. 4d). Furthermore, the peak of S–O at 168.3 eV is observed which may be due to the surface oxidation of Co-Mn-Cu-S HPNDAs [41].

The pore structure of the as-obtained Co-Mn-Cu-S HPNDAs, Co-S NDAs, Co-Cu-S HPNDAs and Co-Mn-S HPNDAs was then investigated by N_2 adsorption/desorption tests. As demonstrated in Fig. 4e and Fig. S10, all the N_2 adsorption/desorption curves reveal

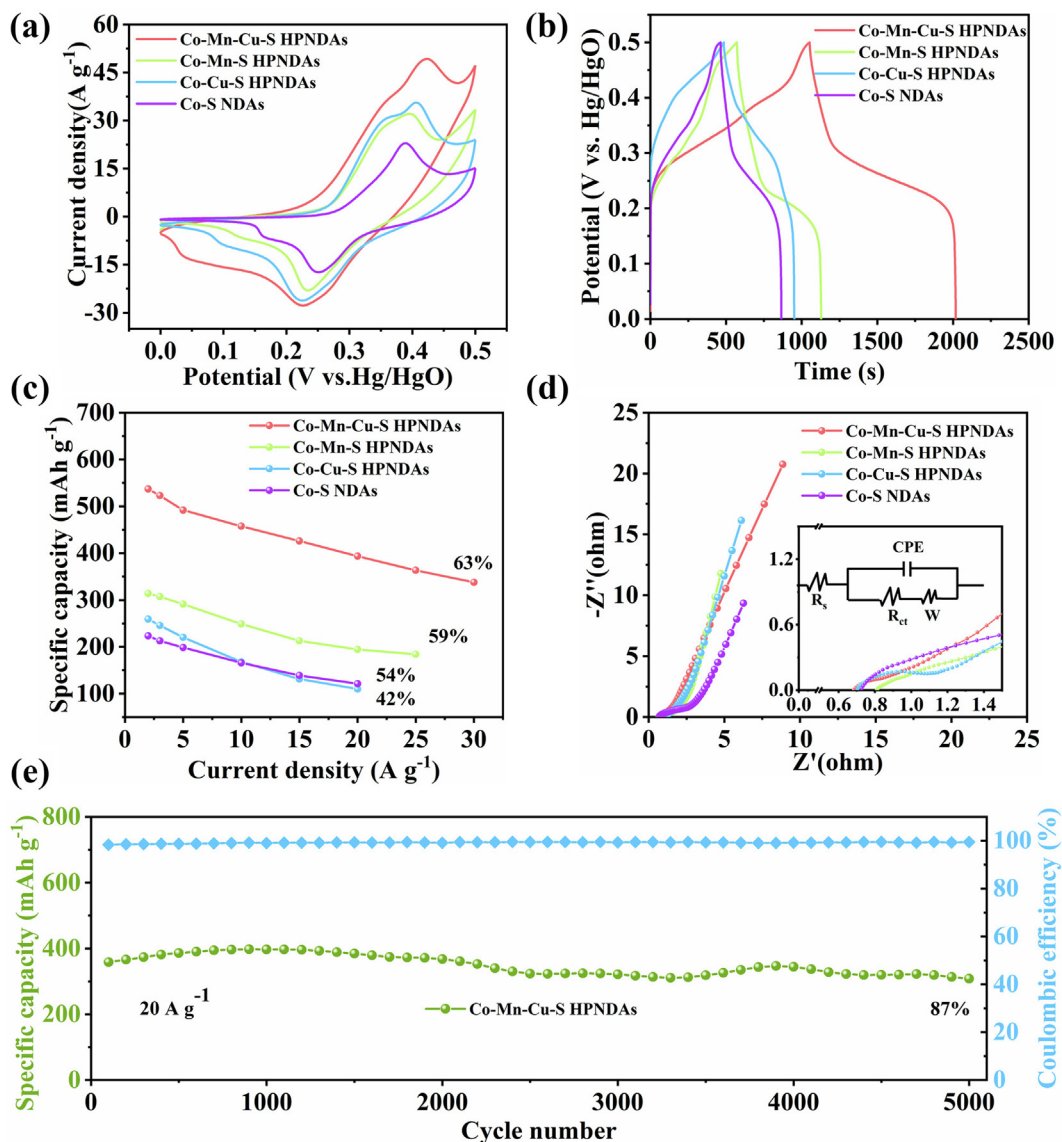
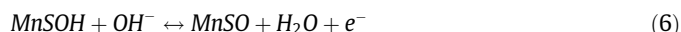
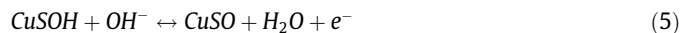
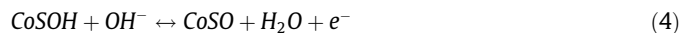
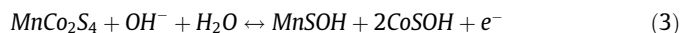
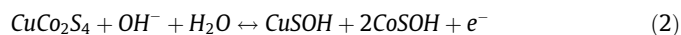
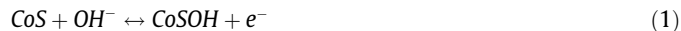


Fig. 5. Electrochemical performances of the Co-Mn-Cu-S HPNDAs, Co-Mn-S HPNDAs, Co-Cu-S HPNDAs and Co-S NDAs. (a) CV curves at 10 mV s^{-1} , (b) GCD curves at 2 A g^{-1} , (c) Specific capacities at different current densities, (d) EIS spectra. (e) Cycling stability and coulombic efficiency of the Co-Mn-Cu-S HPNDAs at a current density of 20 A g^{-1} .

the typical Type I isotherms with a hysteresis loop, indicating the coexistence of micropores and mesopores in the samples. The hierarchical porous structure of the Co-Mn-Cu-S HPNDAs can also be certified by the pore size distribution curve, in which the micropores are centered at 0.9 nm , while the mesopores are focused on 5.6 nm and 23.2 nm (Fig. 4f). The coexistence of micropores and mesopores can boost the physical adsorption of electrolytes and facilitate the mass transport. Thus, Co-Mn-Cu-S HPNDAs with the unique hierarchical porosity achieve a high Brunauer-Emmett-Teller (BET) surface area of $615 \text{ m}^2 \text{ g}^{-1}$, which are higher than the Co-S NDAs ($405 \text{ m}^2 \text{ g}^{-1}$). The large BET surface area is beneficial for the exposure of more active sites to electrolytes to enhance the electrochemical reactions.

The electrochemical performances of the as-prepared Co-Mn-Cu-S HPNDAs, Co-S NDAs, Co-Cu-S HPNDAs and Co-Mn-S HPNDAs samples were first studied in the three-electrode configuration. As shown in Fig. 5a, all the cyclic voltammogram (CV) curves show a potential window of $0\text{--}0.5 \text{ V}$ and a pair of redox peaks, indicating the redox behavior of the hybrids. The possible electrochemical reactions are shown as follows [33,42–44].



The integral area of the CV curve and peak current response of Co-Mn-Cu-S HPNDAs are significantly larger than those of others, suggesting the superior electrochemical performance of Co-Mn-Cu-S HPNDAs. Such results can also be verified by the longest discharge time of Co-Mn-Cu-S HPNDAs in the galvanostatic charge-discharge (GCD) curves (Fig. 5b). Fig. 5c presents the GCD curves of the four samples at different current densities from 2 to 30 A g^{-1} . The Co-Mn-Cu-S HPNDAs electrode delivers a much higher specific capacity of 536.8 mAh g^{-1} (3865 F g^{-1}) at 2 A g^{-1} com-

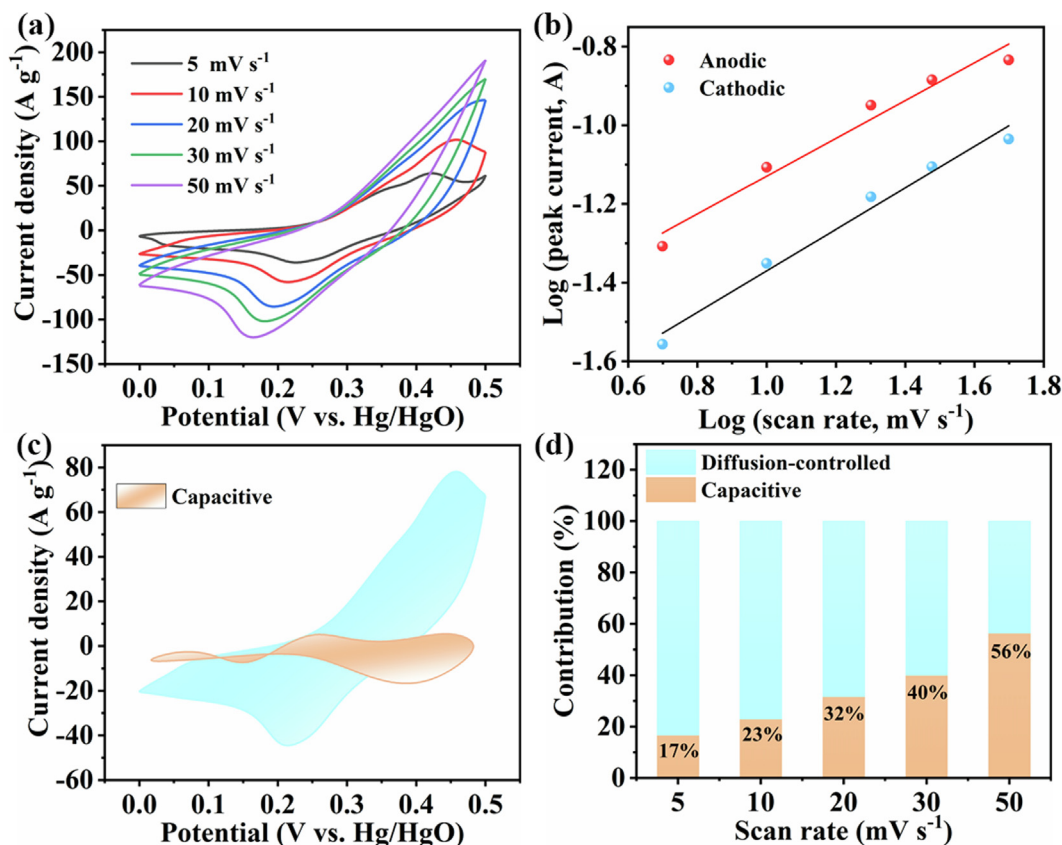


Fig. 6. (a) CV curves of the Co-Mn-Cu-S HPNDAs at different scan rates. (b) The plot of $\log(i)$ versus $\log(v)$. (c) Separation of the diffusion and capacitive-controlled currents of Co-Mn-Cu-S HPNDAs at a scan rate of 10 mV s^{-1} . (d) Relative contribution of the diffusion and capacitive-controlled charge storage at different scan rates.

pared to 223.5 mAh g^{-1} (1609 F g^{-1}) of Co-S NDAs, 259.1 mAh g^{-1} (1866 F g^{-1}) of Co-Cu-S HPNDAs, and 309.8 mAh g^{-1} (2230 F g^{-1}) of Co-Mn-S HPNDAs. The value is also superior to other reported electrode materials based on transition metal sulfides (Table S2). In addition, a good rate performance with 63% capacity retention can be obtained for Co-Mn-Cu-S HPNDAs when the current density increases from 2 to 30 A g^{-1} . The value also surpasses those of Co-Cu-S HPNDAs (42%), Co-Mn-S HPNDAs (59%) and Co-S NDAs (54%) electrodes. The superior capacity and rate capability of Co-Mn-Cu-S HPNDAs are due to the synergistic effect of ternary cobalt, manganese, copper incorporation and the hierarchical porous structure.

The reaction kinetics of the different samples was assessed using electrochemical impedance spectra (EIS) measurements. As presented in Fig. 5d, all Nyquist plots are composed of two parts: a semicircle in high frequency region and a straight line in the low frequency region. The smaller semicircle in high frequency region and higher slope in low frequency region of Co-Mn-Cu-S HPNDAs demonstrate a lower charge transfer resistance (R_{ct}) and faster ion diffusion kinetics, respectively. Furthermore, long cycling stability is also a pivotal factor to assess the electrochemical performance of electrode materials. As shown in Fig. 5e and Fig. S11, Co-Mn-Cu-S HPNDAs can maintain 87% of the initial capacity after 5000 cycles, which exceeds Co-S (34%) and reveals its robust electrochemical stability. The initial increase of specific capacity at the first 1000 cycles may be due to the gradual permeation of electrolytes into the electrodes to activate the materials [25].

The detailed energy storage mechanism was deeply researched via CV measurements. As shown in Fig. 6a, the anodic and cathodic peaks move to the positive potential and negative potential with the increase of the scan rate, respectively, which can be attributed to the polarization effect [45]. Moreover, all the CV curves present

similar shape even at a high scan rate of 50 mV s^{-1} , demonstrating superior reversibility and rate capability. The relationship between peak current (i) and scan rate (v) can be used to investigate the reaction kinetics [46,47]:

$$i = av^b \quad (7)$$

where a and b stand for constants. When the value of b equals 1.0, representing a surface capacitive controlled process, while it is closely related to the diffusion-controlled reaction when the value of b equals 0.5 [48]. For Co-Mn-Cu-S HPNDAs, the b -values of cathodic and anodic peak are 0.57 and 0.53, respectively, suggesting a diffusion-controlled behavior (Fig. 6b). The respective contributions of capacitive controlled and diffusion-controlled processes to the total charge storage can be obtained through the following equation [49]:

$$i(V) = k_1 v + k_2 v^{1/2} \quad (8)$$

where $i(V)$ stands for the response current, v is the scan rate, k_1 and k_2 are constants. As shown in Fig. 6d, the diffusion-controlled process contributes 83% of the entire capacity at 5 mV s^{-1} . It decreases with the increase of scan rate because of the limited diffusion of ions into the bulk [50].

On the basis of the foregoing, the superior electrochemical performance of Co-Mn-Cu-S HPNDAs can be attributed to the following aspects. For the one hand, the incorporation of Mn and Cu in cobalt sulfides can provide more active sites and introduce a synergistic effect to boost the redox reactions. For the other hand, the 3D hierarchical porous structure is beneficial for the penetration of electrolytes and thus accelerates the ion diffusion kinetics.

To assess the potential of Co-Mn-Cu-S HPNDAs in practical application, the quasi-solid-state HSC device was assembled with

Co-Mn-Cu-S HPNDAs as the positive electrode, MOF-derived NPC as the negative electrode, and polyvinyl alcohol (PVA)-KOH gel as the electrolyte. As shown in Fig. S12, the NPC electrode exhibits a specific capacitance of 371 F g^{-1} at 1 A g^{-1} . Fig. 7a shows CV curves of the Co-Mn-Cu-S HPNDAs//NPC HSC with potential windows, which indicates that the potential windows of the device can be extended to 1.5 V without evident polarization. The CV curves all display the quasi-rectangular shape at different scan rate from 5 to 100 mV s^{-1} , indicating the good match between positive and negative electrodes (Fig. 7b). As demonstrated in Fig. 7c, GCD curves of the HSC device present a good symmetry shape, implying its excellent electrochemical reversibility. As a result, a maximum specific capacity of 205 F g^{-1} at 1 A g^{-1} and superb rate performance with 63% of the capacity retention are reached for the HSC device (Fig. 7d). The energy and power densities of the Co-Mn-Cu-S HPNDAs//NPC HSC are plotted in Fig. 7e. The HSC device delivers a maximum energy density of 63.8 W h kg^{-1} at a power density of 743 W kg^{-1} and even maintained 40 W h kg^{-1} at a

power density of 9.7 kW kg^{-1} , which are superior to the recently reported transition metal sulfide-based devices, such as $\text{CuCo}_2\text{S}_4\text{-HNN//AC}$ (44.1 W h kg^{-1} at 800 W kg^{-1}) [51], $\text{Co}_2\text{CuS}_4\text{/NG//NG}$ (53.3 W h kg^{-1} at 795 W kg^{-1}) [52], $\text{MnCo}_2\text{S}_4\text{/rGO}$ (31.3 W h kg^{-1} at 800 W kg^{-1}) [13], $\text{MnCo}_2\text{S}_4\text{/CC//PCP/rGO}$ (43 W h kg^{-1} at 801 W kg^{-1}) [53], $\text{NiCo}_2\text{S}_4\text{//AC}$ (44.8 W h kg^{-1} at 790 W kg^{-1}) [54], $\text{NiCo}_2\text{S}_4\text{/NCF//OMC/NCF}$ (45.5 W h kg^{-1} at 510 W kg^{-1}) [55], $\text{CoS}_x\text{/C//PCNFs}$ (15 W h kg^{-1} at 413 W kg^{-1}) [56], $\text{Co}_3\text{S}_4\text{//AC}$ (54.8 W h kg^{-1} at 400 W kg^{-1}) [57], $\text{Co}_3\text{S}_4\text{/CoMo}_2\text{S}_4\text{//AC}$ (33.1 W h kg^{-1} at 850 W kg^{-1}) [58], $\text{Co}_9\text{S}_8\text{-QD//C}$ (56.4 W h kg^{-1} at 880 W kg^{-1} , Table S3) [59]. Moreover, the HSC device can maintain 5000 cycles without obvious loss in capacity at 10 A g^{-1} , further indicating the out-standing cycling stability (Fig. 7f). Also, the results are comparable to those of other transition-metal sulfide-based HSCs (Table S3). The superior electrochemical performances of the Co-Mn-Cu-S HPNDAs//NPC HSC device endow it with great potential in practical energy storage application and two HSCs con-

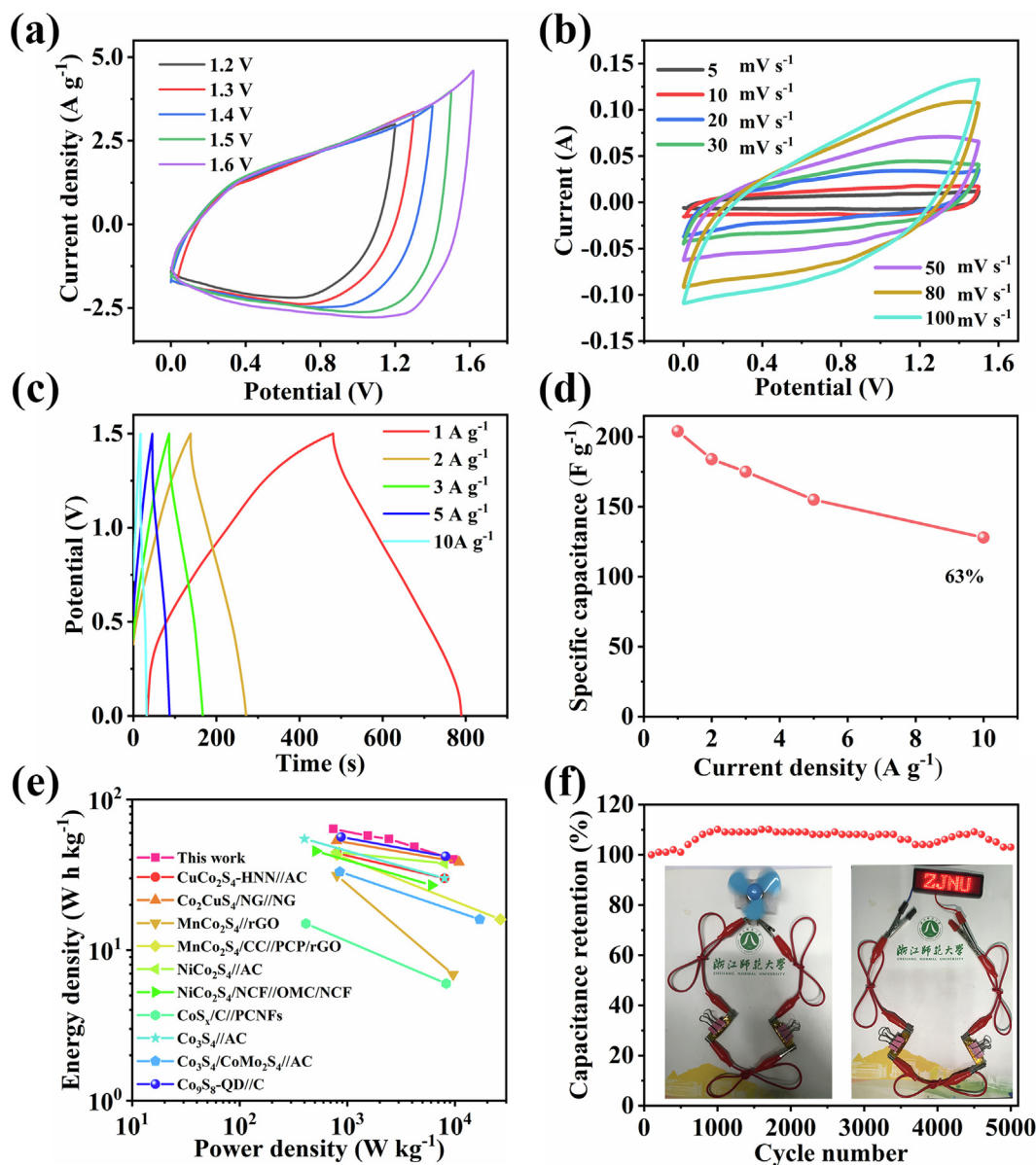


Fig. 7. Electrochemical performances of the Co-Mn-Cu-S HPNDAs//NPC HSC. (a) CV curves at the scan rate of 20 mV s^{-1} with different potential windows. (b) CV curves at different scan rates from 5 to 100 mV s^{-1} . (c) GCD curves at different current densities from 1 to 10 A g^{-1} . (d) Specific capacities at different current densities. (e) Ragone plots compared with other HSCs. (f) Cycling stability at the current density of 10 A g^{-1} .

nected in series can lighten the LED lights and make a small fan work easily.

4. Conclusion

In summary, a facile self-templated strategy has been developed to fabricate ternary Co-Mn-Cu-S HPNDAs on NF as an advanced electrode for HSC. Owing to the structural merits and synergistic effect of ternary Co-Mn-Cu-S components, the Co-Mn-Cu-S HPNDAs electrode exhibits an ultrahigh capacity of 536.8 mAh g⁻¹ at 2 A g⁻¹ and out-standing rate performance with 63% capacity retention from 2 to 30 A g⁻¹. In addition, when assembled for a quasi-solid-state HSC, the energy density reaches 63.8 Wh kg⁻¹ and a long cycle life of 5000 cycles is acquired. These results all demonstrate the great potential of multiple-transition-metal chalcogenides with sophisticated structures for high-performance HSCs.

CRedit authorship contribution statement

Wuquan Ye: Conceptualization, Formal analysis, Writing – review & editing. **Pengcheng Ye:** Investigation, Methodology. **Haiyan Wang:** Data curation, Methodology, Investigation, Writing – review & editing. **Fang Chen:** Conceptualization, Methodology. **Yijun Zhong:** Formal analysis. **Yong Hu:** Conceptualization, Supervision, Funding acquisition, Writing – review & editing.

Declaration of Competing Interest

The authors declare that they have no known competing financial interests or personal relationships that could have appeared to influence the work reported in this paper.

Acknowledgements

This work is financially supported by the Major Program of Zhejiang Provincial Natural Science Foundation of China (LD22B030002), Zhejiang Provincial Ten Thousand Talent Program and the Independent Designing Scientific Research Project of Zhejiang Normal University (2020ZS03).

Appendix A. Supplementary data

Supplementary data to this article can be found online at <https://doi.org/10.1016/j.jcis.2021.12.159>.

References

- [1] C. Choi, D.S. Ashby, D.M. Butts, R.H. DeBlock, Q. Wei, J. Lau, B. Dunn, Achieving high energy density and high power density with pseudocapacitive materials, *Nat. Rev. Mater.* 5 (1) (2020) 5–19.
- [2] H. Wang, W. Ye, Y. Yang, Y. Zhong, Y. Hu, Zn-ion hybrid supercapacitors: Achievements, challenges and future perspectives, *Nano Energy* 85 (2021) 105942.
- [3] L. Kouchachvili, W. Yaici, E. Entchev, Hybrid battery/supercapacitor energy storage system for the electric vehicles, *J. Power Sources* 374 (2018) 237–248.
- [4] N. Choudhary, C. Li, J. Moore, N. Nagaiah, L. Zhai, Y. Jung, J. Thomas, Asymmetric supercapacitor electrodes and devices, *Adv. Mater.* 29 (2017) 1605336.
- [5] Y. Shao, M.F. El-Kady, J. Sun, Y. Li, Q. Zhang, M. Zhu, H. Wang, B. Dunn, R.B. Kaner, Design and mechanisms of asymmetric supercapacitors, *Chem. Rev.* 118 (18) (2018) 9233–9280.
- [6] Y. Yang, D. Chen, H. Wang, P. Ye, Z. Ping, J. Ning, Y. Zhong, Y. Hu, Two-step nitrogen and sulfur doping in porous carbon dodecahedra for Zn-ion hybrid supercapacitors with long term stability, *Chem. Eng. J.* (2021), <https://doi.org/10.1016/j.cej.2021.133250>.
- [7] W. Lu, J. Shen, P. Zhang, Y. Zhong, Y. Hu, X.W. Lou, Construction of CoO/Co-Cu-S hierarchical tubular heterostructures for hybrid supercapacitors, *Angew. Chem. Int. Ed.* 58 (43) (2019) 15441–15447.
- [8] H. Wang, Y. Yang, Q. Li, W. Lu, J. Ning, Y. Zhong, Z. Zhang, Y. Hu, Molecule-assisted modulation of the high-valence Co³⁺ in 3D honeycomb-like Co_xS_y networks for high-performance solid-state asymmetric supercapacitors, *Sci. China Mater.* 64 (2021) 840–851.
- [9] Y. Zhu, X. Ji, Z. Wu, Y. Liu, NiCo₂S₄ hollow microsphere decorated by acetylene black for high-performance asymmetric supercapacitor, *Electrochim. Acta* 186 (2015) 562–571.
- [10] D. Zha, Y. Fu, L. Zhang, J. Zhu, X. Wang, Design and fabrication of highly open nickel cobalt sulfide nanosheets on Ni foam for asymmetric supercapacitors with high energy density and long cycle-life, *J. Power Sources* 378 (2018) 31–39.
- [11] J. Huang, J. Wei, Y. Xiao, Y. Xu, Y. Xiao, Y. Wang, L. Tan, K. Yuan, Y. Chen, When Al-doped cobalt sulfide nanosheets meet nickel nanotube arrays: a highly efficient and stable cathode for asymmetric supercapacitors, *ACS Nano* 12 (2018) 3030–3041.
- [12] W. Lu, Y. Yang, T. Zhang, L. Ma, X. Luo, C. Huang, J. Ning, Y. Zhong, Y. Hu, Synergistic effects of Fe and Mn dual-doping in Co₃S₄ ultrathin nanosheets for high-performance hybrid supercapacitors, *J. Colloid Interf. Sci.* 590 (2021) 226–237.
- [13] S. Liu, S.C. Jun, Hierarchical manganese cobalt sulfide core-shell nanostructures for high-performance asymmetric supercapacitors, *J. Power Sources* 342 (2017) 629–637.
- [14] J. Du, Q. Yan, Y. Li, K. Cheng, K.e. Ye, K. Zhu, J. Yan, D. Cao, X. Zhang, G. Wang, Hierarchical copper cobalt sulfides nanowire arrays for high-performance asymmetric supercapacitors, *Appl. Surf. Sci.* 487 (2019) 198–205.
- [15] Y. Zhu, X. Ji, H. Chen, L. Xi, W. Gong, Y. Liu, The investigation of the electrochemically supercapacitive performances of mesoporous CuCo₂S₄, *RSC Adv.* 6 (87) (2016) 84236–84241.
- [16] L. Wang, Y. Han, X. Feng, J. Zhou, P. Qi, B. Wang, Metal-organic frameworks for energy storage: Batteries and supercapacitors, *Coord. Chem. Rev.* 307 (2016) 361–381.
- [17] H. Furukawa, K.E. Cordova, M. O’Keeffe, O.M. Yaghi, The chemistry and applications of metal-organic frameworks, *Science* 341 (2013) 1230444.
- [18] S. Dang, Q.-L. Zhu, Q. Xu, Nanomaterials derived from metal-organic frameworks, *Nat. Rev. Mater.* 3 (2017) 17075.
- [19] Q. Wang, F. Gao, B. Xu, F. Cai, F. Zhan, F. Gao, Q. Wang, ZIF-67 derived amorphous CoNi₂S₄ nanocages with nanosheet arrays on the shell for a high-performance asymmetric supercapacitor, *Chem. Eng. J.* 327 (2017) 387–396.
- [20] C. Qu, L. Zhang, W. Meng, Z. Liang, B. Zhu, D. Dang, S. Dai, B. Zhao, H. Tabassum, S. Gao, H. Zhang, W. Guo, R. Zhao, X. Huang, M. Liu, R. Zou, MOF-derived α-NiS nanorods on graphene as an electrode for high-energy-density supercapacitors, *J. Mater. Chem. A* 6 (9) (2018) 4003–4012.
- [21] Q. Yang, Y.u. Liu, L. Xiao, M. Yan, H. Bai, F. Zhu, Y. Lei, W. Shi, Self-templated transformation of MOFs into layered double hydroxide nanoarrays with selectively formed Co₉S₈ for high-performance asymmetric supercapacitors, *Chem. Eng. J.* 354 (2018) 716–726.
- [22] K. Tao, X. Han, Q. Cheng, Y. Yang, Z. Yang, Q. Ma, L. Han, A zinc cobalt sulfide nanosheet array derived from a 2D bimetallic metal-organic frameworks for high-performance supercapacitors, *Chem. Eur. J.* 24 (48) (2018) 12584–12591.
- [23] D. Guo, X. Song, L. Tan, H. Ma, H. Pang, X. Wang, L. Zhang, Metal-organic framework template-directed fabrication of well-aligned pentagon-like hollow transition-metal sulfides as the anode and cathode for high-performance asymmetric supercapacitors, *ACS Appl. Mater. Inter.* 10 (49) (2018) 42621–42629.
- [24] C. Yang, M. Shi, X. Song, X. Zhao, L. Zhao, J. Liu, P. Zhang, L. Gao, A robust hierarchical microcapsule for efficient supercapacitors exhibiting an ultrahigh current density of 300 A g⁻¹, *J. Mater. Chem. A* 6 (14) (2018) 5724–5732.
- [25] Z. Yuan, H. Wang, J. Shen, P. Ye, J. Ning, Y. Zhong, Y. Hu, Hierarchical Cu₂S@NiCo-LDH double-shelled nanotube arrays with enhanced electrochemical performance for hybrid supercapacitors, *J. Mater. Chem. A* 8 (42) (2020) 22163–22174.
- [26] J. Zhang, T. Zhang, D. Yu, K. Xiao, Y. Hong, Transition from ZIF-L-Co to ZIF-67: A new insight into the structural evolution of zeolitic imidazolate frameworks (ZIFs) in aqueous systems, *CrystEngComm* 17 (2015) 8212–8215.
- [27] X. Han, K. Tao, D. Wang, L. Han, Design of a porous cobalt sulfide nanosheet array on Ni foam from zeolitic imidazolate frameworks as an advanced electrode for supercapacitors, *Nanoscale* 10 (6) (2018) 2735–2741.
- [28] H. Xuan, Y. Guan, X. Han, X. Liang, Z. Xie, P. Han, Y. Wu, Hierarchical MnCo-LDH/rGO@NiCo₂S₄ heterostructures on Ni foam with enhanced electrochemical properties for battery-supercapacitors, *Electrochim. Acta* 335 (2020) 135691.
- [29] J.-J. Zhou, X. Han, K. Tao, Q. Li, Y.-L. Li, C. Chen, L. Han, Shish-kebab type MnCo₂O₄@Co₃O₄ nanoneedle arrays derived from MnCo-LDH@ZIF-67 for high-performance supercapacitors and efficient oxygen evolution reaction, *Chem. Eng. J.* 354 (2018) 875–884.
- [30] J. Yu, Q. Wang, D. O’Hare, L. Sun, Preparation of two dimensional layered double hydroxide nanosheets and their applications, *Chem. Soc. Rev.* 46 (19) (2017) 5950–5974.
- [31] X. Zhang, C. Si, X. Guo, R. Kong, F. Qu, A MnCo₂S₄ nanowire array as an earth-abundant electrocatalyst for an efficient oxygen evolution reaction under alkaline conditions, *J. Mater. Chem. A* 5 (33) (2017) 17211–17215.
- [32] M. Sun, J. Tie, G. Cheng, T. Lin, S. Peng, F. Deng, F. Ye, L. Yu, In situ growth of burl-like nickel cobalt sulfide on carbon fibers as high-performance supercapacitors, *J. Mater. Chem. A* 3 (4) (2015) 1730–1736.
- [33] K. Le, M. Gao, W. Liu, J. Liu, Z. Wang, F. Wang, V. Murugadoss, S. Wu, T. Ding, Z. Guo, MOF-derived hierarchical core-shell hollow iron-cobalt sulfides nanoarrays on Ni foam with enhanced electrochemical properties for high

- energy density asymmetric supercapacitors, *Electrochim. Acta* 323 (2019) 134826.
- [34] H. Guan, P. Cai, X. Zhang, Y. Zhang, G. Chen, C. Dong, Cu₂O templating strategy for the synthesis of octahedral Cu₂O@Mn(OH)₂ core-shell hierarchical structures with a superior performance supercapacitor, *J. Mater. Chem. A* 6 (28) (2018) 13668–13675.
- [35] Y. Zhang, C. Liu, B. Xu, F. Qi, W. Chu, Degradation of benzotriazole by a novel fenton-like reaction with mesoporous Cu/MnO₂: Combination of adsorption and catalysis oxidation, *Appl. Catal. B: Environ.* 199 (2016) 447–457.
- [36] X. Zhao, M. Deng, G. Rao, Y. Yan, C. Wu, Y. Jiao, A. Deng, C. Yan, J. Huang, S. Wu, W. Chen, T. Lei, P. Xu, W. He, J. Xiong, High-performance SERS substrate based on hierarchical 3D Cu nanocrystals with efficient morphology control, *Small* 14 (2018) 1802477.
- [37] S. Cai, D. Zhang, L. Shi, J. Xu, L. Zhang, L. Huang, H. Li, J. Zhang, Porous Ni-Mn oxide nanosheets in situ formed on nickel foam as 3D hierarchical monolith de-NO_x catalysts, *Nanoscale* 6 (13) (2014) 7346–7353.
- [38] X. Guo, T. Zheng, G. Ji, N. Hu, C. Xu, Y. Zhang, Core/shell design of efficient electrocatalysts based on NiCo₂O₄ nanowires and NiMn LDH nanosheets for rechargeable zinc-air batteries, *J. Mater. Chem. A* 6 (22) (2018) 10243–10252.
- [39] L. Yan, Y. Ren, X. Zhang, Y. Sun, J. Ning, Y. Zhong, B. Teng, Y. Hu, Electronic modulation of composite electrocatalysts derived from layered NiFeMn triple hydroxide nanosheets for boosted overall water splitting, *Nanoscale* 11 (43) (2019) 20797–20808.
- [40] Q. Li, Z. Xing, D. Wang, X. Sun, X. Yang, In situ electrochemically activated CoMn-S@NiO/CC nanosheets array for enhanced hydrogen evolution, *ACS Catal.* 6 (5) (2016) 2797–2801.
- [41] Y. Wang, Q. Du, H. Zhao, S. Hou, Y. Shen, H. Li, X. Kong, W. Sun, B.o. Zhang, S. Li, F. Huo, W. Zhang, Metal-organic framework derived leaf-like CoSNC nanocomposites for supercapacitor electrodes, *Nanoscale* 10 (37) (2018) 17958–17964.
- [42] J. Zhu, S. Tang, J. Wu, X. Shi, B. Zhu, X. Meng, Wearable high-performance supercapacitors based on silver-sputtered textiles with FeCo₂S₄-NiCo₂S₄ composite nanotube-built multitripod architectures as advanced flexible electrodes, *Adv. Energy Mater.* 7 (2017) 1601234.
- [43] H. You, L. Zhang, Y. Jiang, T. Shao, M. Li, J. Gong, Bubble-supported engineering of hierarchical CuCo₂S₄ hollow spheres for enhanced electrochemical performance, *J. Mater. Chem. A* 6 (13) (2018) 5265–5270.
- [44] Y. Huang, F. Cui, J. Bao, Y. Zhao, J. Lian, T. Liu, H. Li, MnCo₂S₄/FeCo₂S₄ “lollipop” arrays on a hollow n-doped carbon skeleton as flexible electrodes for hybrid supercapacitors, *J. Mater. Chem. A* 7 (36) (2019) 20778–20789.
- [45] M. Liang, M. Zhao, H. Wang, J. Shen, X. Song, Enhanced cycling stability of hierarchical NiCo₂S₄@Ni(OH)₂@ppy core-shell nanotube arrays for aqueous asymmetric supercapacitors, *J. Mater. Chem. A* 6 (6) (2018) 2482–2493.
- [46] Q. Li, W. Lu, Z. Li, J. Ning, Y. Zhong, Y. Hu, Hierarchical MoS₂/NiCo₂S₄@C urchin-like hollow microspheres for asymmetric supercapacitors, *Chem. Eng. J.* 380 (2020) 122544.
- [47] S. Liu, Y. Yin, K.S. Hui, K.N. Hui, S.C. Lee, S.C. Jun, High-performance flexible quasi-solid-state supercapacitors realized by molybdenum dioxide@nitrogen-doped carbon and copper cobalt sulfide tubular nanostructures, *Adv. Sci.* 5 (2018) 1800733.
- [48] H.-S. Kim, J.B. Cook, H. Lin, J. Ko, S. Tolbert, V. Ozolins, B. Dunn, Oxygen vacancies enhance pseudocapacitive charge storage properties of MoO_{3-x}, *Nat. Mater.* 16 (4) (2017) 454–460.
- [49] S. Wang, Y. Shao, W. Liu, Y. Wu, X. Hao, Elastic sandwich-type GaN/MnO₂/MnON composites for flexible supercapacitors with high energy density, *J. Mater. Chem. A* 6 (27) (2018) 13215–13224.
- [50] R. Wang, C. Xu, J.-M. Lee, High performance asymmetric supercapacitors: New NiOOH nanosheet/graphene hydrogels and pure graphene hydrogels, *Nano Energy* 19 (2016) 210–221.
- [51] S.E. Moosavifard, S. Fani, M. Rahmanian, Hierarchical CuCo₂S₄ hollow nanoneedle arrays as novel binder-free electrodes for high-performance asymmetric supercapacitors, *Chem. Commun.* 52 (24) (2016) 4517–4520.
- [52] M. Guo, J. Balamurugan, T.D. Thanh, N.H. Kim, J.H. Lee, Facile fabrication of Co₂CuS₄ nanoparticle anchored N-doped graphene for high-performance asymmetric supercapacitors, *J. Mater. Chem. A* 4 (44) (2016) 17560–17571.
- [53] A.M. Elshahawy, X. Li, H. Zhang, Y. Hu, K.H. Ho, C. Guan, J. Wang, Controllable MnCo₂S₄ nanostructures for high performance hybrid supercapacitors, *J. Mater. Chem. A* 5 (16) (2017) 7494–7506.
- [54] Y. Liu, Z. Wang, Y. Zhong, M. Tade, W. Zhou, Z. Shao, Molecular design of mesoporous NiCo₂O₄ and NiCo₂S₄ with sub-micrometer-polyhedron architectures for efficient pseudocapacitive energy storage, *Adv. Funct. Mater.* 27 (2017) 1701229.
- [55] L. Shen, J. Wang, G. Xu, H. Li, H. Dou, X. Zhang, NiCo₂S₄ nanosheets grown on nitrogen-doped carbon foams as an advanced electrode for supercapacitors, *Adv. Energy Mater.* 5 (2015) 1400977.
- [56] Y. Liu, J. Zhou, W. Fu, P. Zhang, X. Pan, E. Xie, In situ synthesis of CoS₂@carbon core-shell nanospheres decorated in carbon nanofibers for capacitor electrodes with superior rate and cycling performances, *Carbon* 114 (2017) 187–197.
- [57] M. Liang, M. Zhao, H. Wang, Q. Zheng, X. Song, Superior cycling stability of a crystalline/amorphous Co₃S₄ core-shell heterostructure for aqueous hybrid supercapacitors, *J. Mater. Chem. A* 6 (43) (2018) 21350–21359.
- [58] X. Yang, H. Sun, P. Zan, L. Zhao, J. Lian, Growth of vertically aligned Co₃S₄/CoMo₂S₄ ultrathin nanosheets on reduced graphene oxide as a high-performance supercapacitor electrode, *J. Mater. Chem. A* 4 (48) (2016) 18857–18867.
- [59] Q. Yang, Q. Wang, Y. Long, F. Wang, L. Wu, J. Pan, J. Han, Y. Lei, W. Shi, S. Song, In situ formation of Co₉S₈ quantum dots in MOF-derived ternary metal layered double hydroxide nanoarrays for high-performance hybrid supercapacitors, *Adv. Energy Mater.* 10 (2020) 1903193.